Chapter 19
Scanning Tunneling Microscopy

Ada Della Pia and Giovanni Costantini

Abstract The Nobel Prize-awarded invention of the scanning tunneling microscope (STM) has profoundly revolutionized contemporary science and technology. The STM has enabled individual atoms and molecules to be imaged, probed and handled with an unprecedented precision, thereby essentially contributing to our current understanding of the world at the nanoscale. Together with its offspring, the atomic force microscope (AFM), the STM is considered as the main innovation behind the birth of nanotechnology. This chapter is an elementary introduction to STM and to its most recent uses. Topics include a basic treatment of the underlying theory of tunneling, the description of the most commonly used experimental setups, a survey of the atomic-scale spectroscopic capabilities (scanning tunneling spectroscopy, STS) and an overview of atomic manipulation experiments.

19.1 Introduction

If a bias voltage is applied to two electrodes a few tenths of a nm apart, a current flows between them even though they are not in contact. This is due to the quantum mechanical process of electron tunneling. The resulting current depends exponentially on the electrode separation s so that even minute, subatomic variations in s produce measurable current changes. In 1981 Gerd Binnig and Heinrich Rohrer at IBM in Zürich realized that by shaping one of the electrodes as a sharp tip and scanning it across the surface of the other (Fig. 19.1), quantum tunneling can be used to build a microscope with ultra high spatial resolution [1]. Moreover, since the current depends also on the electronic properties of the electrodes, they recognized that this microscope has the ability to probe the electronic density of states of surfaces at the atomic scale. A few years later, Don Eigler at IBM in Almaden, showed that, due to the extremely localized interaction between tip and sample, it is even possible to use

A. Della Pia · G. Costantini (✉)
Department of Chemistry, The University of Warwick, Gibbet Hill Road, Coventry CV4 7AL, UK
e-mail: g.costantini@warwick.ac.uk

A. Della Pia
e-mail: A.della-pia@warwick.ac.uk

G. Bracco, B. Holst (eds.), *Surface Science Techniques*,
Springer Series in Surface Sciences 51, DOI 10.1007/978-3-642-34243-1_19,

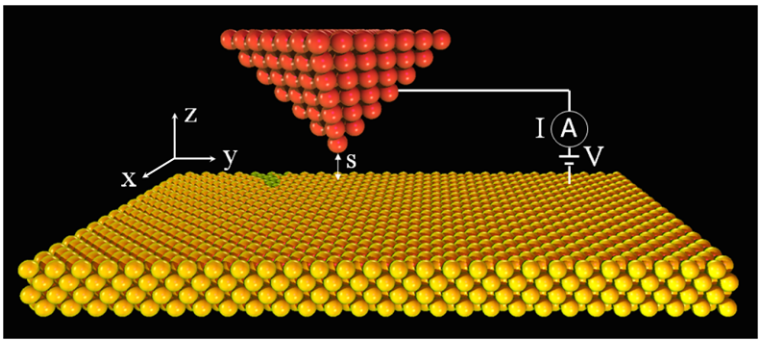

Fig. 19.1 Schematic representation of a STM. Tip and sample are held at a distance s of a few tenths of a nm and a bias voltage V, up to a few Volts, is applied between them. The resulting tunneling current I is recorded while the tip is moved across the surface. The coordinate system is also shown

this instrument to manipulate individual atoms, to position them at arbitrary locations and therefore to build artificial structures atom-by-atom [2]. This remarkable achievement brought to reality the visionary predictions made by Richard Feynman in his famous 1959 lecture "*There's plenty of room at the bottom*" [3].

The construction of this instrument, dubbed the scanning tunneling microscope (STM), was awarded the 1986 Nobel Prize in Physics and has revolutionized contemporary science and technology. The STM has enabled individual atoms and molecules to be imaged, probed and handled with an unprecedented precision, thereby essentially contributing to our current understanding of the world at the nanoscale. Together with its offspring, the atomic force microscope (AFM), the STM is considered as the main innovation behind the birth of nanotechnology.

This chapter is an elementary introduction to STM and to its most recent uses. It starts with a discussion of the physical principles and processes at the basis of STM in Sect. 19.2. This is followed by a description of the experimental setup and the technical requirements needed for actually operating such an instrument in Sect. 19.3. Section 19.4 is dedicated to the most frequent use of STM, namely imaging of surfaces, while Sect. 19.5 gives an account of its spectroscopic possibilities. Finally, Sect. 19.6 surveys the atomic manipulation capabilities of STM.

19.2 Theory of Tunneling

Figure 19.2 is a schematic representation of the energy landscape experienced by an electron when moving along the z axis of a metallic-substrate/insulator/metallic-tip tunneling junction. Usually the tip and the sample are not made of the same material and are therefore characterized by different work functions, ϕ_T and ϕ_S, respectively. At equilibrium, the two metals have a common Fermi level, resulting in an electric

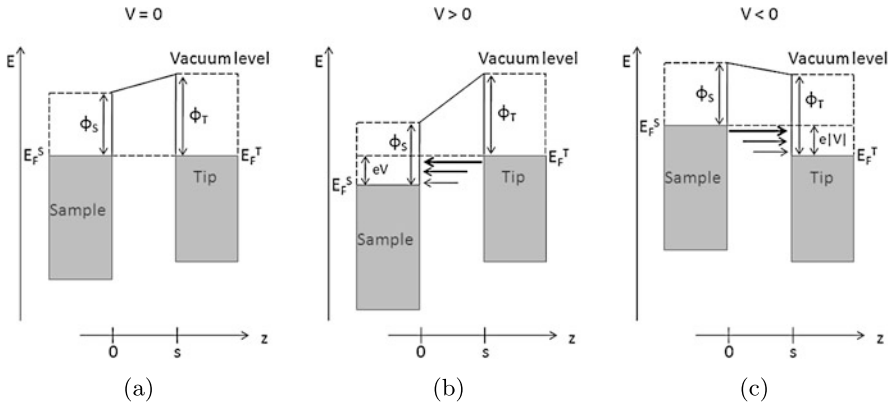

Fig. 19.2 Energy potential perpendicular to the surface plane for an electron in a tip-vacuum-sample junction. z is the surface normal direction, and s is the tip-sample distance. The *gray boxes* represent the Fermi-Dirac distribution at 0 K. $\phi_{T,S}$ and $E_F^{T,S}$ are the work functions and the Fermi levels of tip and sample, respectively. (**a**) Tip and sample in electrical equilibrium: a trapezoidal potential barrier is created. (**b**) Positive sample bias: the electrons tunnel from occupied states of the tip into unoccupied states of the sample. The thickness and the length of the *arrows* indicate the exponentially decreasing probability that an electron with the corresponding energy tunnels through the barrier. (**c**) Negative sample bias

field being established across the gap region and in different local vacuum levels, depending on the difference $\phi_T - \phi_S$ (Fig. 19.2(a)). Since the work functions in metals are of the order of several eV, the potential in the gap region is typically much higher than the thermal energy kT and thus acts as a barrier for sample and tip electrons. A classical particle cannot penetrate into any region where the potential energy is greater than its total energy because this requires a negative kinetic energy. However, this is possible for quantum mechanical objects such as electrons which are described by delocalized wave functions. This phenomenon goes under the name of *quantum tunneling*. In an unpolarized tip-sample junction the electrons can tunnel from the tip to the sample and vice versa, but there is no net tunneling current. On the contrary, if a voltage V is applied between sample and tip,[1] the Fermi level of the former is shifted by $-eV$ and a net tunneling current occurs, whose direction depends on the sign of V (Figs. 19.2(b) and (c)).

The tunneling current can be evaluated by following the time-dependent perturbation approach developed by Bardeen [4, 5]. The basic idea is to consider the isolated sample and tip as the unperturbed system described by the stationary one-particle Schrödinger equations:

$$(\mathcal{T} + \mathcal{U}_S)\psi_\mu = E_\mu \psi_\mu \tag{19.1}$$

[1] Here the convention is adopted to take the tip as a reference since experimentally the voltage is often applied to the sample while the tip is grounded. If V is the bias voltage, the energy for an electron in the sample will change by $-eV$, i.e. it will decrease for positive values of V.

and

$$(\mathcal{T} + \mathcal{U}_T)\chi_\nu = E_\nu \chi_\nu, \tag{19.2}$$

where $\mathcal{T}$ is the electron kinetic energy and ψ_μ and χ_ν are the unperturbed wave functions. The electron potentials $\mathcal{U}_S$ and $\mathcal{U}_T$ are non-zero only in the sample and in the tip, respectively. Based on this, it can be shown [5] that the transition probability per unit time $w_{\mu\nu}$ of an electron from the sample state ψ_μ to the tip state χ_ν is given by the Fermi golden rule:

$$w_{\mu\nu} = \frac{2\pi}{\hbar}|M_{\mu\nu}|^2 \delta(E_\nu - E_\mu), \tag{19.3}$$

where the matrix element is:

$$M_{\mu\nu} = \int \chi_\nu^*(\boldsymbol{x})\mathcal{U}_T(\boldsymbol{x})\psi_\mu(\boldsymbol{x})\, d^3\boldsymbol{x}. \tag{19.4}$$

The δ function in (19.3) implies that the electrons can tunnel only between levels with equal energy, that is, (19.3) accounts only for an elastic tunneling process.[2] The total current is obtained by summing $w_{\mu\nu}$ over all the possible tip and sample states and by multiplying this by the electron charge e. The sum over the states can be changed into an energy integral by considering the density of states (DOS) $\rho(E)$:

$$\sum_{\mu,\nu} \to 2 \int f(\epsilon)\rho(\epsilon)\, d\epsilon. \tag{19.5}$$

The factor 2 accounts for the spin degeneracy while f, the Fermi-Dirac distribution function, takes into consideration Pauli's exclusion principle and the electronic state population at finite temperatures. As a consequence, the total current can be written as:

$$\begin{aligned} I = \frac{4\pi e}{\hbar} \int_{-\infty}^{\infty} &\left[f_T\left(E_F^T - eV + \epsilon\right) - f_S\left(E_F^S + \epsilon\right)\right] \\ &\times \rho_T\left(E_F^T - eV + \epsilon\right)\rho_S\left(E_F^S + \epsilon\right)|M|^2\, d\epsilon, \end{aligned} \tag{19.6}$$

where E_F is the Fermi energy and the indexes T and S refer to the tip and the sample, respectively. Expression (19.6) already accounts for the movement of electrons from the sample to the tip and vice versa.

Several approximations can be made to simplify (19.6) and to obtain an analytically manageable expression for I. If the thermal energy $k_B T \ll eV$, the Fermi-Dirac distributions can be approximated by step functions and the total current reduces to:[3]

$$I = \frac{4\pi e}{\hbar} \int_0^{eV} \rho_T\left(E_F^T - eV + \epsilon\right)\rho_S\left(E_F^S + \epsilon\right)|M|^2\, d\epsilon. \tag{19.7}$$

[2] The case of an inelastic tunneling process will be considered in Sect. 19.5.7.

[3] Expression (19.7) is valid only for $V > 0$. For $V < 0$ the integrand remains identical but the integration limits become $-e|V|$ and 0.

In this case only electrons with an energy differing from E_F by less than eV can participate to the tunneling current. This can be directly seen in Fig. 19.2(b) for the case of positive sample bias: tip electrons whose energy is lower than $E_F^T - eV$ cannot move because of Pauli's exclusion principle, while there are no electrons at energies higher than E_F^T.

The main problem in determining expression (19.6) is, however, the calculation of the tunneling matrix elements M since this requires a knowledge of the sample and the tip wave functions, which can be very complicated. On the other hand, for relatively small bias voltages (in the ± 2 V range), Lang [6] showed that a satisfactory approximation is obtained by considering that the tunneling current flows only between the last atom of a perfectly sharp tip and the surface atom directly underneath. In this case $|M|^2$ is given by a simple one-dimensional WKB tunneling probability. In the WKB approximation [7], the probability $D(\epsilon)$ that an electron with energy ϵ tunnels through a potential barrier $U(z)$ of arbitrary shape is expressed as:

$$D(\epsilon) = \exp\left\{-\frac{2}{\hbar}\int_0^s \left[2m\big(U(z)-\epsilon\big)\right]^{\frac{1}{2}} dz\right\}. \tag{19.8}$$

This semiclassical approximation is applicable if $\epsilon \ll U$ which is in general satisfied in the case of metal samples where the work function is of the order of several eV. In order to obtain a simple analytical expression for D, the trapezoidal potential barrier of a biased tip-sample junction (see Figs. 19.2(b) and (c)) is further approximated with a square barrier of average height

$$\phi_{eff}(V) = (\phi_T + \phi_S + eV)/2. \tag{19.9}$$

By using this, expression (19.8) becomes:

$$D(\epsilon, V, s) = \exp\left[-2s\sqrt{\frac{2m}{\hbar^2}\left(\frac{\phi_T+\phi_S}{2} + \frac{eV}{2} - \epsilon\right)}\right] = \exp(-2ks), \tag{19.10}$$

where

$$k = \sqrt{\frac{2m}{\hbar^2}(\phi_{eff} - \epsilon)}. \tag{19.11}$$

The inverse decay length $2k$ dictates how sensitive the tunneling current is on variations of the tip-sample separation s and is therefore essential in determining the spatial resolution of STM. In order to evaluate k, it must be noted that electrons closest to the Fermi level experience the lowest potential barrier and are therefore characterized by an exponentially larger tunneling probability (see Figs. 19.2(b) and (c)). Thus, in a first approximation, it can be assumed that only these electrons contribute to the tunneling current which, for positive bias, is equivalent to set $\epsilon \approx eV$ in (19.11). Moreover, if the bias is much smaller than the work functions, eV can be neglected in (19.9), resulting in

$$k \cong \frac{\sqrt{m(\phi_T+\phi_S)}}{\hbar} = 5.1\sqrt{\frac{\phi_T+\phi_S}{2}}\ \text{nm}^{-1}, \tag{19.12}$$

where the work functions are expressed in eV. Using typical numbers for metallic work functions, the value of the inverse decay length $2k$ in (19.10) becomes of the

order of 20 nm^{-1}. Therefore, variations in s of 0.1 nm correspond to one order of magnitude changes in the tunneling probability and, as a consequence, in the measured current. This very high sensitivity provides the STM with a vertical resolution in the picometer regime.

The lateral resolution of STM depends on how different points of the tip contribute to the total tunneling current. By considering a spherical tip shape with radius R, most of the current originates from the central position since this is closest to the surface. A point laterally displaced by Δx from the tip center is $\Delta z \approx \frac{\Delta x^2}{2R}$ further away from the substrate (higher order Δx terms are neglected in this evaluation). As a consequence, with respect to the tip center, the corresponding tunneling probability is reduced by a factor:

$$\exp\left(-2k\frac{\Delta x^2}{2R}\right). \tag{19.13}$$

By considering a tip radius $R \approx 1$ nm, the current changes by one order of magnitude for variations $\Delta x = 0.3$ nm. The actual lateral resolution is typically smaller than this upper limit and can reach down to fractions of an Å. Its specific value however depends on the precise shape of the tip which is unknown a priori. These values, together with the vertical resolution discussed above, lie at the basis of the STM atomic imaging capabilities.

Finally, by following the approximation by Lang [6], the tunneling probability (19.10) can be substituted for the tunneling matrix $|M|^2$ in (19.7) and the total tunneling current becomes:

$$I = \frac{4\pi e}{\hbar}\int_0^{eV} \rho_T\left(E_F^T - eV + \epsilon\right)\rho_S\left(E_F^S + \epsilon\right)e^{-2ks}\,d\epsilon. \tag{19.14}$$

Therefore, for a fixed lateral position of the tip above the sample, the tunneling current I depends on the tip-sample distance s, the applied voltage V and the tip and sample density of states ρ_T and ρ_S, respectively.

It should be noted that, due to the 1D approximation [6], the densities of states ρ_T and ρ_S in (19.14) do not refer to the whole tip and sample but only to the last atom of the tip and to the atom of the sample which is located directly underneath. For this reason ρ_S does depend on the lateral position of the tip (x, y) and will be referred to as local density of states (LDOS).

19.3 Experimental Setup

As seen in the previous section, variations of 0.1 nm in s induce changes in the tunneling probability of one order of magnitude. The exponential dependence in (19.10) lies at the heart of the ultimate spatial resolution of STM but places stringent requirements on the precision by which s must be controlled, as well as on the suppression of vibrational noise and thermal drift. Moreover, typical tunneling currents are in the 0.01–10 nA range, requiring high gain and low noise electronic components. The following subsections are dedicated to a general overview of technologies and methods employed to meet these specifications.

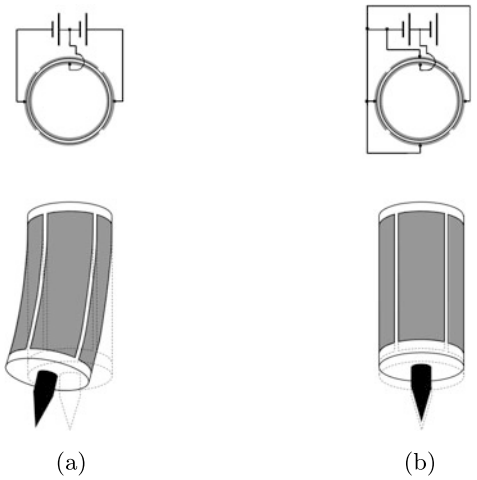

Fig. 19.3 Piezoelectric scanner tube. (**a**) Schematic representation of the lateral tip displacement and (**b**) of the vertical retraction and corresponding electrical wiring (*upper row*)

19.3.1 Scanner and Coarse Positioner

The operation of a STM requires extremely fine movements of the tip relative to the sample which are realized by the use of piezoelectric ceramic actuators (*scanners*). These expand or retract depending on the voltage difference applied to their ends and, in a first approximation, the voltage-expansion relation is linear with a proportionality factor (piezo constant) usually of few nanometer/Volt. The main requirements for a good scanner are: high mechanical resonance frequencies, so as to minimize noise vibrations in the frequency region where the feedback electronics operates (see Sect. 19.3.2); high scan speeds; high spatial resolution; decoupling between x, y and z motions; minimal hysteresis and creep; low thermal drift. Although several types of STM scanner have been developed, including the bar or tube tripod, the unimorph disk and the bimorph [8], the most frequently used is a single piezoelectric tube whose outer surface is divided into four electrode sections of equal area (Fig. 19.3). By applying opposite voltages between the inner electrode and opposite sections of the outer electrode, the tube bends and a lateral displacement is obtained (Fig. 19.3(a)). The z motion is realized by polarizing with the same voltage the inner electrode in respect to all four outer electrodes (Fig. 19.3(b)). By applying several hundred Volts to the scanner, lateral scan widths up to 10 μm and vertical ones up to 1 μm can be obtained, while retaining typical lateral and vertical resolutions of 0.1 nm and 0.01 nm, respectively.

While scanning is typically done by one individual piezoelectric element, larger displacements up to several millimeters are needed to bring the tip in close proximity to the sample, to move it to different regions of the surface or to exchange samples or tips. These are achieved by mounting the scanner onto a coarse position device. Several designs have been developed to this aim including:

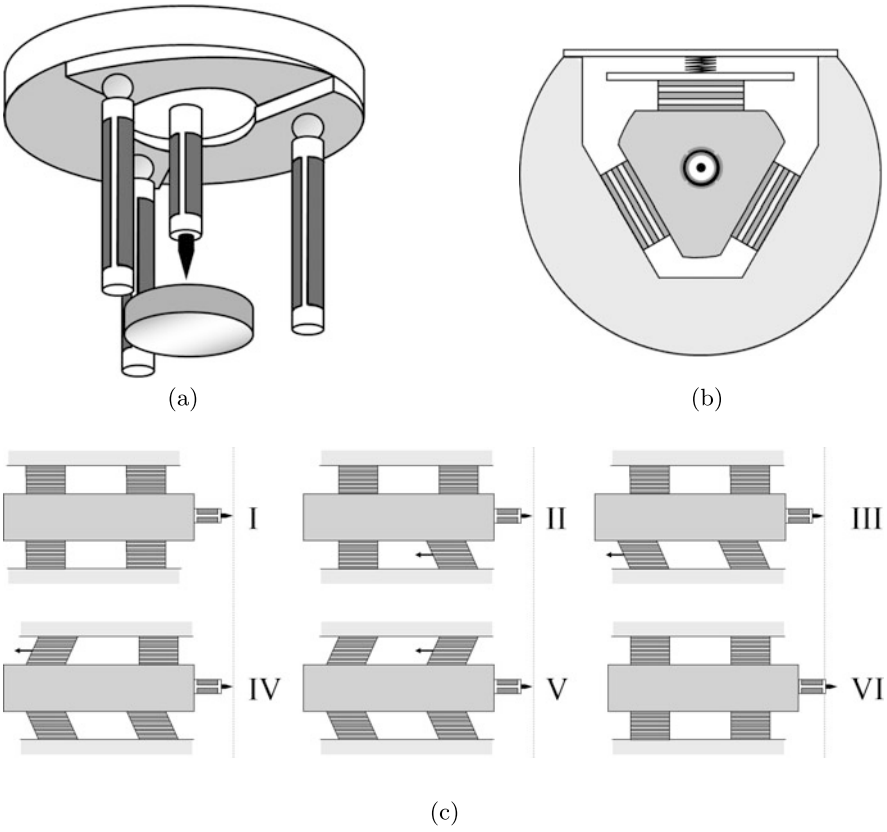

Fig. 19.4 (**a**) Schematic representation of the Besocke-beetle scanner. (**b**) Section view of the Pan motor as viewed from the tip and (**c**) schematics of its working principle

- Micrometer screws driven either manually or by a stepper motor. Mechanical coupling and thermal drift due to the heat generated by the mechanism limit the function of these devices.
- Piezoelectric walkers like the louse used in the first STM [9] or the inchworm [10], composed by two piezoelectric feet and a piezoelectric body. The movement is obtained by alternating the clamping of the first foot, the contraction or expansion of the body and the clamping of the second foot.
- Magnetic walkers where the movement is obtained by applying voltage pulses to a coil with a permanent magnet inside.
- Piezoelectric driven stick-slip motors, as the Besocke-beetle [11] or the Pan motor [12]. Together with the inchworm walker, these two latter are the most frequently used in modern commercial instruments.

The Besocke-beetle consists of a base plate with three 120° sections of a shallow ramp which is supported, through ball bearings, by three outer piezo tubes (Fig. 19.4(a)). A further piezo tube which carries the tip and acts as scanner is

located in the center of the plate. Coarse lateral tip displacements are realized by using the three outer piezoelectric tubes and operating them in a linear stick-slip motion with respect to the base plate [11]. Coarse vertical displacements are achieved by inducing a rotational stick-slip motion of the piezos: because of the ramps, the rotation is coupled with a vertical motion, similar to the effect of a screw thread. A STM head based on the Besocke design has the advantage of being thermally compensated since the coarse positioning device and the scanner are made of the same components and can thus be expected to have the same thermal expansion coefficients. However, its drawbacks are a substantial bulkiness and the reduced overall coarse z travel (typically less than 1 mm).

In the motor developed by S.H. Pan and coworkers [12] the tip tube scanner is mounted onto a prism-shaped sapphire (Fig. 19.4(b)). A spring mechanism holds the prism inside a ceramic body by firmly pressing it against six piezo stacks which are used to perform coarse z movements (Fig. 19.4(b)). One step forward of the prism is achieved by sequentially applying six sharp high-voltage steps to the individual piezo stacks so that these bend backwards one at a time without moving the prism which is hold by the remaining ones (slip motion, steps II to V in Fig. 19.4(c)). In the final step, all voltages are slowly reduced to zero so that the piezo stacks simultaneously relax back to their neutral positions and, through friction, move the prism forward (stick motion, step VI in Fig. 19.4(c)). The Pan motor has a very long z travel (typically up to 10 mm) and, being particularly compact and of reduced size, it is the solution of choice for STMs operating at mK temperatures and in high magnetic fields.

19.3.2 Electronics and Control System

The voltage signals driving the piezoelectric actuators and their temporal succession and duration are generated by an electronic control system. The electronics are also used to bias the tunneling junction, to record the tunneling current and to generate the STM images. In most of the modern instruments these tasks are digitally implemented by a computer interfaced with digital to analog (DAC) and analog to digital (ADC) converters. The tunneling current is amplified by a high gain I–V converter (10^8–10^{10} V/A) usually positioned in close proximity of the tip, so as to reduce possible sources of electronic interference. This signal is then acquired by an ADC and processed by the control system. DACs are used to apply the bias voltage (from a few mV to a few V) between tip and sample and, in conjunction with high voltage amplifiers, to polarize the piezo elements. A feedback loop is integrated into the control system and is activated during the frequently used *constant current* imaging mode (see Sect. 19.4). By acting on the z motion of the scanner, the feedback varies s to keep the tunneling current constant. This is controlled by a proportional-integral and derivative (PID) filter whose parameters can be set by the operator.

Finally, a lock-in amplifier is often used in scanning tunneling spectroscopy (STS) experiments for improving the signal-to-noise ratio and for directly isolating

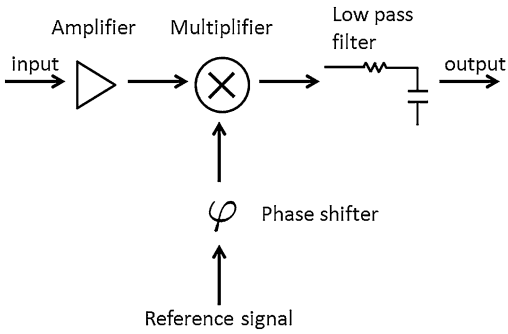

Fig. 19.5 Schematic block diagram of a lock-in amplifier

the first or second order derivative of the current with respect to the voltage. These are directly related to the electronic properties of the samples (see Sect. 19.5). In the I(V) spectroscopy technique (see Sect. 19.5.1) a small high-frequency sinusoidal signal $V_m = V_0 \sin(\omega t + \varphi_0)$ is summed to the bias voltage V applied between tip and sample (typical values of V_0 are between 1 and 100 mV, while ω is usually a few kHz). Since the amplitude of the sinusoidal signal V_0 is small, the tunneling current resulting from (19.14) can be expanded in a power series:

$$I\big(V + V_0 \sin(\omega t + \varphi_0)\big) = I(V) + \frac{dI(V)}{dV} V_0 \sin(\omega t + \varphi_0) + \frac{d^2 I(V)}{dV^2} \frac{V_0^2}{2} \sin^2(\omega t + \varphi_0) + \cdots . \quad (19.15)$$

In a lock-in amplifier, schematized in Fig. 19.5, the amplified current is multiplied by a sinusoidal reference signal V_{ref} and then integrated over a time longer than its period. All the components in expression (19.15) with a frequency different from the reference signal are filtered out by this last step since the integral of their product with V_{ref} is averaged to 0. As a consequence, if V_{ref} has the same frequency as the modulation signal, the only remaining part is a DC signal proportional to the amplitude of the ω-component in (19.15), i.e. to $(dI/dV)\cos(\varphi - \varphi_0)$, where φ is the phase of the reference signal. By adjusting φ so that $\varphi - \varphi_0 = 0$, the output of the lock-in amplifier is maximized and the differential conductivity is obtained at the voltage V. Similarly, if V_{ref} is chosen to have a frequency 2ω, only the second harmonic component in (19.15) survives the integration step, resulting in a signal proportional to d^2I/dV^2.

19.3.3 Tip

Sharp metal tips with a low aspect ratio are essential to optimize the resolution of the STM images and to minimize flexural vibrations, respectively. Ideally, in order to obtain atomically resolved topographies and accurate spectroscopic measurements, the tip should be terminated by a single atom. In this case, because of the strong dependence on the tip-sample separation (see Sect. 19.2), most of the tunneling current

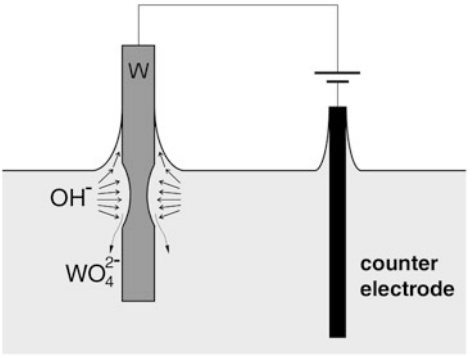

Fig. 19.6 Schematics of the electrochemical cell used for the etching of W tips in a strong alkaline solution

would originate from the last atom whose position and local DOS would precisely determine the tunneling conditions. In practice however, it is almost impossible to determine the exact atomic configuration of the tip and the actual current is often due to a number of different atoms. This is still compatible with good tunneling conditions as long as these atoms are sufficiently localized (in order to avoid "multiple tip effects") and if their structural and chemical state remains constant during scanning. An overview of the possible artifacts in STM imaging due to the tip shape can be found in [13].

The most commonly used methods to produce STM tips are to manually cut or to electrochemically etch thin wires of platinum-iridium and tungsten, respectively. These materials are chosen because of their hardness, in order to prevent tips becoming irreversible damaged after an accidental crash.[4] Due to their chemical inertness, Pt-Ir tips are often used to scan in air on atomically flat surfaces without the need of any further processing. However, they typically have inconsistent radii, while etched W tips are characterized by a more reproducible shape. These latter have the drawback that a surface oxide up to 20 nm thick is formed during etching or exposure to air [14]. For this reason W tips are primarily employed in ultra high vacuum (UHV) where the oxide layer can be removed through ion sputtering and annealing cycles.

The most used etching method is the so-called DC drop-off where the wire is immersed in a concentrated aqueous alkaline solution and the etching occurs largely at the air-electrolyte interface (Fig. 19.6). A constant positive voltage is applied between the wire (anode) and a counter electrode (cathode) inducing two reactions: the water reduction in bubbles of hydrogen gas and OH^- ions at the cathode, and the oxidative dissolution of the solid W anode to soluble tungstate ions [15]. The shape of the meniscus limits the diffusion of the OH^- ions and therefore reduces their concentration in its upper part. This slows down the etching of the wire in this region. On the other hand, also the part of the wire below the meniscus is etched at a slower rate because it is shielded by the downwards flow of tungstate ions (Fig. 19.6). The combination of these two effects leads to the typical hyperboloid

[4]Other metallic elements and even semiconductor materials have been used as tips for specific STM applications.

shape of a DC etched tip. When the weight of the immersed portion of the wire exceeds its tensile strength, the wire breaks and the actual tip is formed. In order to avoid a tip blunting, it is essential that the etching stops immediately after the wire breaks. This can be achieved by using an electronic control system that records the etching current and switches off the voltage if the current diminishes below a set threshold.

Prior to use, tips are often checked by optical microscopy, scanning electron microscopy, field ion microscopy or transmission electron microscopy. The quality of a tip can be further improved during scanning by using "*tip forming*" procedures, including pulsing and controlled crashing into metal surfaces. These processes work because they might remove molecules adsorbed on the tip or coat the tip itself with atoms of the metallic substrate, thereby producing a more stable tip apex.

If STM is performed in polar liquids, electrochemical processes might generate Faradaic or non-Faradaic currents which can be of the same order of magnitude or even larger than the tunneling current. In order to minimize these effects, the tip, except for its very apex, must be coated with an insulating material [16].

19.3.4 Vibration Isolation

A low level of mechanical noise is an essential requirement for any type of scanning probe microscopy. For this reason the core of a STM, where the tip-sample junction is located, is always equipped with one or several types of vibration damping systems. These can be stacks of metal plates separated by elastic spacers, suspension springs or eddy current dampers composed of copper elements and permanent magnets. The low frequency components of mechanical noise (< 10 Hz), which are the most difficult to eliminate, are minimized by building a small and rigid STM with a high resonance frequency. Depending on the overall size and weight of the microscope, further noise damping strategies can be adopted. Smaller, typically ambient conditions STMs, can be placed on metal or granite slabs suspended by springs or bungee cords or floating on pneumatic isolators. Sometimes, piezo-driven, feedback-controlled active vibration suppressors are also combined with passive systems. Larger versions of pneumatic isolators and active damping are used to float the frames and the chambers of big UHV STMs. The laboratory where a STM instrument is located also plays an essential role for its performance. Ground floor rooms are always preferred since they minimize low-frequency natural building oscillations, which can be very difficult to counteract. High resolution instruments are sometimes placed on large concrete blocks which are separated from the rest of the laboratory floor and rest either on a sand bed, an elastomer barrier or on second-stage pneumatic isolators [8]. Moreover, they are also often surrounded by an acoustically insulating box. All these systems essentially act as low-pass mechanical filters whose effectiveness improves with decreasing cutoff frequencies, i.e. with increasing mass and decreasing rigidity. For this reason, the body of a STM is typically a relatively heavy block of metal and the frames, slabs and vacuum chambers supporting or containing the microscope often have a considerable weight.

19.3.5 Setups for Different Environments and Temperatures

Different types of STMs have been developed that can operate in various environments such as air, inert atmosphere (N_2, Ar), vacuum, high pressure, liquid or in an electrochemical cell. The core of the different instruments is essentially the same, although the experimental chambers and setups in which they are located can vary substantially. Ambient condition STMs are typically quite compact and rigid and do not need elaborated anti-vibrational mechanisms. On the other hand, since sound waves represent a major problem, atmospheric pressure STMs are usually contained in an acoustic enclosure. A STM operating in vacuum must be hosted in a chamber with vibration-free pumps (typically ionic pumps for UHV) and must be equipped with sophisticated sample and tip manipulation mechanisms. Such systems often also have an *in-situ* surface preparation stage allowing the handling of samples without air exposure.

STM can be performed at high pressures (1–30 bar) by installing the microscope head into gas manifolds under conditions similar to those used in industrial catalytic processes. Also in this case, sample and tip manipulation and preparation stages are mandatory parts of the system. Since these types of studies are typically performed at elevated temperatures (up to 600 K) and in the presence of highly reactive gases, the metallic parts of the STM scanner and of the chamber are often gold plated, the volume of the STM chamber is kept as small as possible and the tip material is chosen to be inert toward the employed gases [17]. Moreover, low voltages are used for polarizing the piezos in order to avoid gas discharges at intermediate pressures (10^{-3}–10 mbar) and shields are added to protect the STM from the deposition of conductive materials which could create electrical shorts.

STM at the liquid/solid interface and electrochemical STM (EC-STM) need the tip and sample to be inside a liquid cell which, in turn, may be placed in a humidity-controlled atmosphere. In the case of low vapor pressure liquids, the STM can be simply operated under ambient conditions by dipping the tip into a liquid droplet deposited on the sample. A special coating must be applied to the tip when working with polar liquids (see Sect. 19.3.3).

STM can also be performed at different temperatures (in vacuum or controlled atmosphere systems): variable temperature STM (VT-STM) able to cover the 5–1400 K range, low temperature STM (LT-STM) operating at 77 K or 5 K and even milli-Kelvin STM instruments are currently available. A VT-STM is typically used to study thermally activated processes such as diffusion and growth, phase transitions, etc. These systems have sample heating and cooling stages which can be operated in a combined way so as to achieve a very precise temperature stabilization. Resistive heating is normally employed to increase the temperature, while both flow and bath cryostats with liquid nitrogen or helium as cryogenic fluids are used to reduce it. Continuous flow cryostats offer a high flexibility in temperature but are characterized by lower thermal stability, by inherent mechanical vibrations and do not easily attain temperatures below 20 K. Bath cryostats are more stable, are able to reach lower temperatures but are often also much bulkier (e.g., in order to limit the He consumption rate, a liquid He cryostat is composed by a double-stage vessel with

an outer liquid nitrogen mantle). For most of these instruments the variable temperature capabilities refer to the possibility of choosing different (fixed) temperatures at which the microscope is run. However, few systems endowed with high performance position tracking and drift compensating capabilities allow a "true" variable temperature operation whereby the same surface area can be imaged with atomic resolution while its temperature is changed. By choosing optimized designs for the piezo scanners and the electronic feedback, video-rate instruments have been developed able to record several tens of images per second and thereby to follow dynamic surface processes such as molecular mobility and assembly in real time [18, 19].

LT-STMs are operated at a fixed temperature and are typically inserted inside double stage cryostats which significantly complicates the tip and sample access. However, these instruments are extremely stable with a very low thermal drift (of the order of tenths of a nm per hour) and are therefore the best choice for STS and manipulation experiments (see Sects. 19.5 and 19.6). Milli-Kelvin STMs enable temperatures to be reached where extremely interesting magnetic, quantum Hall physics and superconductivity phenomena occur. Moreover, the thermal broadening of electronic features is strongly reduced, which is required for high resolution measurements. These systems operate based on the Joule-Thomson evaporative cooling of liquid ^{3}He to temperatures of about 300 mK or liquid ^{3}He and ^{4}He mixtures below 10 mK. The STM heads can be further placed inside large-bore superconducting magnets (at present up to 15 Tesla), allowing the low temperature and high magnetic field conditions necessary to access superconductive phase transitions or to detect single spin flip processes.

19.4 STM Imaging

Since the first STM images of the surfaces of $CaIrSn_4$ and Au [1] were published back in 1982, STM has been used to analyze a wide range of materials: clean and adsorbate covered metal surfaces, semiconductors, superconductors, thin insulating layers, small and large organic molecules, individual atoms, liquid-solid interfaces, magnetic layers and surfaces, quasicrystals, polymers, biomolecules, nanoclusters and carbon nanotubes. Imaging is the most frequent application of STM used to determine the structural properties of substrates and their reconstructions, the presence of defects, sites of adsorption for adatoms and molecules and the symmetry and periodicity of adsorbate superstructures.

STM images are generated by recording the tunneling current as a function of the tip position while the tip is scanned across the sample surface. This can be done in two different ways which define the two main STM imaging modes:

- *Constant height mode*. The z section of the piezo scanner is kept fixed while the tip is moved over the substrate at a constant bias voltage (Fig. 19.7(a)). Variations of the tip-sample distance due to the surface topography produce a corresponding variation of the tunneling current which is recorded point-by-point and used to build the STM gray-level image. This mode is employed only in small areas of

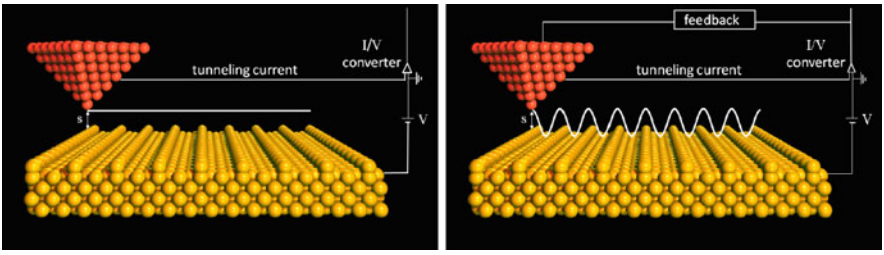

(a) (b)

Fig. 19.7 (**a**) Constant height and (**b**) constant current imaging modes. The *thick lines* represent the trajectory followed by the tip, $s(x, y)$

extremely flat surfaces, where the probability of crashing into protrusions such as steps or defects is relatively small. Very high scanning speeds can be used because of the absence of a feedback control.

- *Constant current mode*. While the x and y sections of the piezo scanner are used to laterally move the tip across the surface, the z section is driven by the electronic feedback so as to maintain a constant tunneling current (Fig. 19.7(b)). The corresponding z-voltage applied to the scanner (feedback signal) is recorded point-by-point and used to build the STM gray-level image. This mode can be employed for any type of surface topography and is therefore the most frequently used.

Since the constant height mode is applied to atomically flat surfaces with sub-Å height variations, the exponential $I - s$ relation derived from (19.14) can be approximated by a linear dependence. As a consequence, constant height STM images are a good representation of flat surfaces. On the other hand, for less planar substrates, the constant current mode must be used which directly reproduces the surface height due to the linear voltage-extension relation of piezoelectric materials. However, even constant current images are a reliable representation of the "true" surface topography only if the sample LDOS does not vary across the scanned area. If this is not the case, a constant current profile corresponds to a complex convolution of topographical and electronic features which can be particularly relevant for surfaces covered with adsorbates.

For example, electronegative atoms like oxygen and carbon can, counter intuitively, appear as depressions in STM images when adsorbed onto metal surfaces [20, 21]. This can be understood by considering the approximation of (19.14) for small voltages and a constant tip density of states:

$$I \propto \rho_S(E_F) \exp(-2ks). \tag{19.16}$$

The chemisorption of electronegative atoms involves a charge transfer from the substrate which is accompanied by the screening of the metal conduction electrons. Both effects yield a decrease of the density of states near the Fermi level compared to the bare metal. As a consequence, in order to keep the product on the right hand side of (19.16) constant, the tip-sample distance s must be reduced, therefore

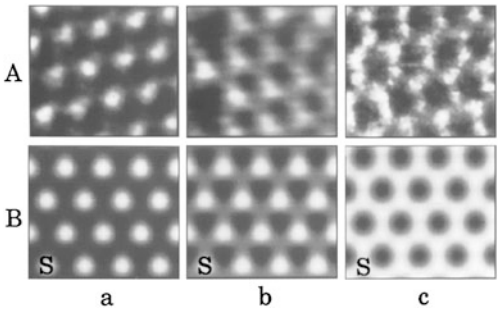

Fig. 19.8 (**A**) STM images for the p(2 × 2) overlayer of sulfur on Re(0001). The sulfur atoms are imaged in three different ways: as circles (**a**), triangles (**b**) or Y shapes (**c**). (**B**) Electron scattering quantum chemical calculations of the STM images with a tip ending in one sulfur atom (**a**), one platinum atom (**b**) or three platinum atoms (**c**). The *letter* S indicates the position of a sulfur atom. Adapted from [24]

producing the observed depression at the position of the adsorbates. A similar phenomenon explains the STM images of acetylene on Cu(001) surfaces, which appears as a dumbbell-shaped depression (see Fig. 19.15(a)) [22].

By using the full transfer Hamiltonian approach, Tersoff and Hamann [23] found that an alternative expression for (19.16) is

$$I \propto \sum_{\nu} \left|\psi_{\nu}(\boldsymbol{r_0})\right|^2 \delta\left(E_{\nu} - E_F^S\right) = \rho_S\left(\boldsymbol{r_0}, E_F^S\right). \tag{19.17}$$

The right hand side of (19.17) represents the number of sample electrons per unit volume and per unity energy calculated at the location of the tip's last atom $\boldsymbol{r_0} = (x, y, s)$ and at the sample Fermi energy. $\rho_S(\boldsymbol{r}, E)$ is often evaluated by means of density functional theory calculations (DFT) and expression (19.17) is used to construct simulated STM constant current images to be directly compared with the experimental ones.

A further critical factor in the STM visualization of adsorbates is the electronic configuration of the tip which is determined by its chemical and structural state. A prominent example of this influence is given by the p(2 × 2) layer of sulfur on Re(0001) [24]. Depending on the tip termination, the sulfur atoms can appear as circles, triangles, or Y-shaped structures in a honeycomb arrangement (upper row in Fig. 19.8). By comparison with theoretical simulations, it was determined that these visualization modes are due to a tip terminating in a single contaminant atom (e.g. S, C), in a single metallic atom (Pt, Rh, Re) or in a trimer of metallic atoms, respectively (lower row in Fig. 19.8) [24].

19.5 Scanning Tunneling Spectroscopy

Besides complicating the interpretation of STM images, the dependence of the tunneling current on the sample DOS also offers the unique opportunity of probing the

electronic characteristics of surfaces with high spatial resolution. Due to the spatial localization of the tunneling current (see Sect. 19.2), STS enables to determine the electronic properties of individual atoms and molecules in relation to their structure, bonding and local environment. By changing the polarity of the bias voltage, STS gives access to both the occupied and the unoccupied states of the sample. In this sense, it is often considered as complementary to ultraviolet photoemission spectroscopy (UPS), inverse photoemission spectroscopy (IPS) and electron energy loss spectroscopy (EELS). While in these latter techniques the signal is averaged over a large surface area (between 0.1 and 2 mm in diameter), STS has the advantage of an ultimate spatial resolution. Moreover, in the case of organic samples, it also avoids possible damaging generated by intense photon or electron beam irradiation. On the other hand, STS does not provide direct chemical information and tip artifacts can strongly influence the spectroscopic data.

Having fixed the tip lateral position, the tunneling current I is a function of the applied bias voltage V and the tip-sample separation s only, the precise relation being established by (19.14). In a STS experiment the relation between two of these three parameters is measured while the remaining one is kept constant.

19.5.1 $I(V)$ Spectroscopy

$I(V)$ spectroscopy, where the tunneling current is measured as a function of the bias voltage for a constant tip-sample separation, is the most widely used technique because it provides indications about the DOS of the sample. However, its extraction from an $I(V)$ curve is a complex procedure since the DOS of the tip and the voltage dependence of the tunneling matrix elements M are usually unknown. As already explained in Sect. 19.2, $|M|^2$ can be approximated for small bias by the WKB tunneling probability D, so to obtain (19.14). By differentiating (19.14) at constant tip-sample distance s, the differential conductance for a positive sample bias is obtained as:

$$\begin{aligned}\frac{dI(V)}{dV} \propto\ & \rho_T\big(E_F^T\big)\rho_S\big(E_F^S+eV\big)D(eV,V,s) \\ & + \int_0^{eV} \rho_T\big(E_F^T-eV+\epsilon\big)\rho_S\big(E_F^S+\epsilon\big)\frac{\partial D(\epsilon,V,s)}{\partial V}\,d\epsilon \\ & + \int_0^{eV} \frac{d\rho_T(E_F^T-eV+\epsilon)}{dV}\rho_S\big(E_F^S+\epsilon\big)D(\epsilon,V,s)\,d\epsilon. \quad (19.18)\end{aligned}$$

The quantity of interest, i.e. the sample LDOS ρ_S, is contained in the first term of (19.18), while the other two terms arise from the voltage dependence of the transmission coefficient D and of the tip DOS ρ_T, respectively. By assuming a constant ρ_T, the third term vanishes. For small bias voltages, the second term provides a smoothly varying background signal since D is a monotonic function of V. Hence, it is often neglected and expression (19.18) is simplified to:

$$\frac{dI(V)}{dV} \propto \rho_S\big(E_F^S+eV\big)D(eV,V,s). \quad (19.19)$$

The monotonous dependence of D on V warrants that any possible structure in dI/dV is due to the voltage dependence of ρ_S. As a consequence, under the assumptions of constant ρ_T and small voltages, the differential conductance can be considered as a good representation of the sample density of states LDOS at the position of the tip.

The voltage dependence of D can however not be neglected for higher biases. In this case, the normalized differential conductivity $(dI/dV)/(I/V)$ is typically a better representation of ρ_S [25]. In fact, both the numerator (dI/dV) and the denominator (I/V) depend on the tunneling probability D and thus, in a first approximation, D cancels out in the ratio. Even if this procedure lacks a strict mathematic foundation, a good agreement has been found between the sample LDOS and the normalized differential conductivity, especially in the case of semiconductors [26]. However, this method cannot be used for wide gap (> 0.5 eV) semiconductors because, close to the band edge, the current approaches zero faster than dI/dV, leading to a divergence in the normalized differential conductivity [27]. A better way of dealing with higher bias values will be presented in Sect. 19.5.2.

The assumption of a constant tip DOS might be a good approximation for a metallic tip but does not hold for tips with adsorbed molecules, either intentionally picked up in a manipulation experiment (see Sect. 19.6) or accidentally transferred during scanning. On the other hand, although usually unknown, the tip DOS remains often unchanged over several subsequential measurements and therefore contributes in the same way to $I(V)$ spectra acquired at different positions on the sample. This allows to develop background subtraction schemes which rely on "calibrating" the tip on a clean spot of the surface and subsequently using this to remove tip-induced features from spectra acquired with the same tip on the objects of interest [28].

$I(V)$ spectroscopy is inherently characterized by an asymmetry in the sensitivity to occupied and unoccupied sample electronic states, the latter being far better visualized than the former. This is due to the transmission through the tunneling barrier which implies that features in ρ_S are enhanced at positive voltages, but are attenuated and difficult to recognize at negative ones. The asymmetry can be easily understood by remembering that, in (19.14), the exponential dependence of D from the bias voltage implies that most of the current is due to electrons tunneling close to the Fermi level. Figure 19.9 illustrates this effect for the case of a featureless ρ_T. At positive voltages (Fig. 19.9(a)), electrons tunnel mainly from the Fermi level of the tip into empty states of the sample. By increasing the voltage, new empty levels of the sample become accessible and, as an increase in V also reduces the tunneling barrier (see (19.10) and Fig. 19.9(b)), the corresponding peaks will be enhanced in the dI/dV spectrum. At a negative bias (Fig. 19.9(c)), the electrons tunnel from the sample E_F to empty tip levels. By decreasing the voltage, (Fig. 19.9(d)), the sample electrons at E_F tunnel into different empty tip states at higher energy but, due to the featureless ρ_T, this does not produce any new structure in the dI/dV spectrum. Any extra peak can only be due to lower-lying filled states of the sample which, however, experience a much larger tunneling barrier and are therefore strongly attenuated (Fig. 19.9(d)).

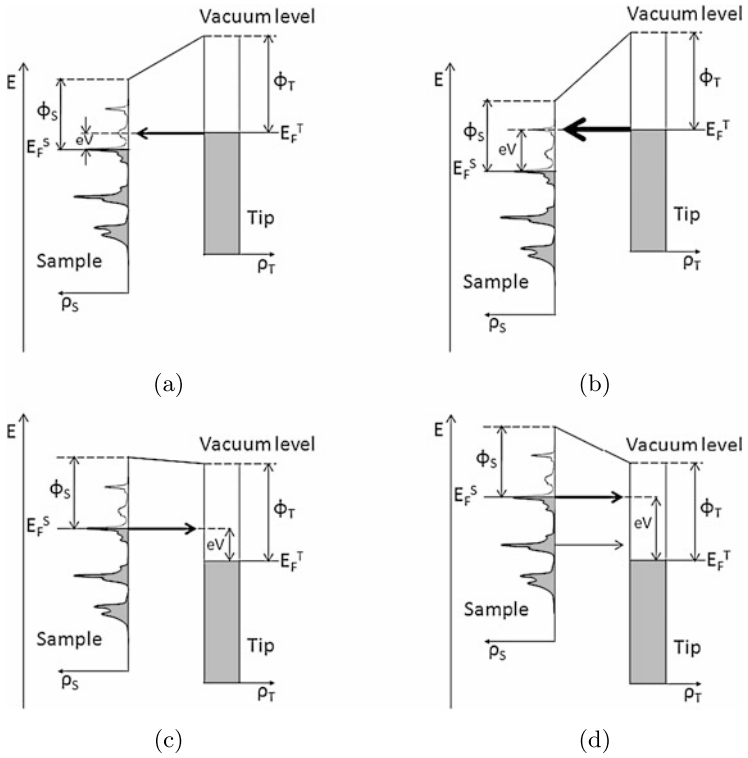

Fig. 19.9 Asymmetry of $I(V)$ spectra in the sensitivity to occupied and unoccupied sample electronic states (see text)

In order to measure an $I(V)$ curve at constant distance, the tip is placed at a certain position of the surface, the feedback is turned off, i.e. the tip-sample distance s is kept fixed, and the voltage is ramped while recording the tunneling current. The slope of the obtained $I(V)$ curve corresponds to the differential conductance between the tip and the sample and, through (19.19), to the sample LDOS. The tip-sample distance s is defined by the so-called *stabilization values*, i.e. by the values of the bias voltage and the tunneling current set before the feedback is turned off. The maximum time available for recording an $I(V)$ spectrum is determined by the actual time that the vertical and lateral position of the tip can be kept fixed with respect to the substrate. These depend on the overall stability of the system and should always be checked before performing a STS measurement. The differential conductivity can be calculated by numerically differentiating the measured $I(V)$ curve. However, this procedure typically results in very noisy conductance values. This problem is managed by measuring directly the differential conductance by means of the lock-in technique as described in Sect. 19.3.2 and Sect. 19.5.2.

19.5.2 Constant-Current Tunneling Spectra

The voltage range that can be explored in an $I(V)$ spectrum at constant s is essentially limited by the exponential dependence of the tunneling probability D on the bias voltage, see (19.10). For changes of V comparable to the work function, the tunneling current strongly increases thereby quickly saturating the high gain I–V converter. Moreover, high current values might become a problem when investigating adsorbed organic molecules which can get altered or even damaged.

An alternative way to determine the sample LDOS which avoids some of these problems is represented by so-called constant-current tunneling spectra where the ramp in V is applied while the feedback regulation is activated. This implies that the control electronics changes the tip-sample distance s as a function of the voltage so as to maintain a constant tunneling current. This procedure avoids any saturation of I and therefore benefits from an increased dynamic range with respect to constant distance $I(V)$ spectroscopy. However, it cannot be applied to spectral regions of low tunneling current, such as bias voltages close to zero or in the band gap of semiconductor materials, since the feedback would simply crash the tip into the sample in the attempt to keep I constant (see (19.14)). Moreover, the use of a lock-in amplifier is a necessary requirement in this technique and not simply a way to improve the signal-to-noise ratio. In fact, the differential conductance can clearly not be obtained by numerically differentiating the $I(V)$ signal, which is constant.

The sample LDOS can however be determined if a high-frequency sinusoidal modulation is added to the slowly varying bias voltage. In fact, if the modulation frequency is higher than the cut-off frequency of the feedback loop, the feedback does not respond to it and reacts only to the quasi-DC variations of the bias. On the other hand, as seen in Sect. 19.3.2, the lock-in amplifier outputs a signal proportional to the differential conductance. Since this occurs for any value of the bias voltage in the ramp, a dI/dV spectrum is effectively generated.

For larger values of the bias voltage V, the second term in (19.18) cannot be neglected any more and, for the case of a constant ρ_T, the correct expression for the differential conductance becomes:

$$\frac{dI[s(V),V]}{dV} \propto \rho_S\left(E_F^S + eV\right) D\left(eV, V, s(V)\right) + \int_0^{eV} \rho_S\left(E_F^S + \epsilon\right) \frac{\partial D(\epsilon, V, s(V))}{\partial V}\, d\epsilon, \tag{19.20}$$

where the dependence of s on V, due to the active feedback, has been explicitly indicated. The derivative of the transmission coefficient D with respect to the bias V can be determined by recalling the 1D WKB expression of D in (19.10). In a first approximation [29], the integral in (19.20) becomes:

$$-\frac{2e\sqrt{2m}s(V)}{\hbar\sqrt{\overline{\phi}}} I(V), \tag{19.21}$$

where $\overline{\phi}$ is the average tip and sample work function. Thus (19.20) can be solved for ρ_S:

$$\rho_S\left(E_F^S + eV\right) = \frac{1}{D(eV, V, s(V))}\left\{\frac{dI[s(V), V]}{dV} + \frac{2e\sqrt{2m}s(V)}{\hbar\sqrt{\overline{\phi}}}I(V)\right\}, \quad (19.22)$$

which is an extension of (19.19). The absolute tip-sample distance, $s(V)$, necessary to determine the sample DOS through (19.22), is typically unknown. However, the simplest way of treating this problem is to consider $s = s_0 + \Delta s(V)$, where $\Delta s(V)$ is the tip excursion which can be measured and s_0 is a reference distance whose value affects the intensity of the peaks in the dI/dV spectrum but not their positions [30]. More sophisticated algorithms have also been proposed to deconvolve the sample DOS from STS measurements based on the 1D-WKB approximation [26, 31, 32]. Alternatively, ρ_S can be directly calculated from measured $I(V)$ curves by numerically inverting (19.14). For example, this approach has been used in order to determine the LDOS of organic nanolayers deposited on a metal surface [33].

19.5.3 CITS

Any type of STS measurement can be done with the same spatial resolution of STM, therefore also on individual molecules or atoms. Moreover, STS can be used to create 2D maps of the sample LDOS with sub-nm resolution. Such measurements are particularly interesting for quantum confined electronic systems (e.g. quantum dots or quantum corrals) or for determining the shape of molecular orbitals (see Sect. 19.5.6) [34]. In current imaging tunneling spectroscopy (CITS), spectroscopic measurements are acquired together with topographical ones, thereby obtaining a much deeper characterization of the sample surface.

There are two main ways to perform CITS. For the first one, the experimental setup is the same as for constant-current tunneling spectroscopy (Sect. 19.5.2), with feedback and lock-in amplifier working simultaneously. However, instead of applying a ramp to the bias voltage, this is kept fixed at a given value V and the tip is scanned across the surface. As a consequence, if the output of the lock-in is plot as a function of the lateral tip position, a 2D map of the differential conductance at eV is generated together with a constant current STM image. The whole spectral information can be retrieved by performing several scans at different V biases. Clearly the same issues discussed in Sect. 19.5.2 arise here when trying to extract the sample LDOS from dI/dV values acquired at different $s(V)$ values.

An alternative CITS method is to record a full $I(V)$ spectrum at constant s for every pixel of a constant current image. This implies first switching off and then reactivating the feedback electronics at each point of the image and is therefore typically a quite long procedure. As a consequence, it is often more practical to take only a STM image and, using this as a reference, to define a sparser grid of points where to measure the $I(V)$ spectra. Even if the stabilization values are identical for

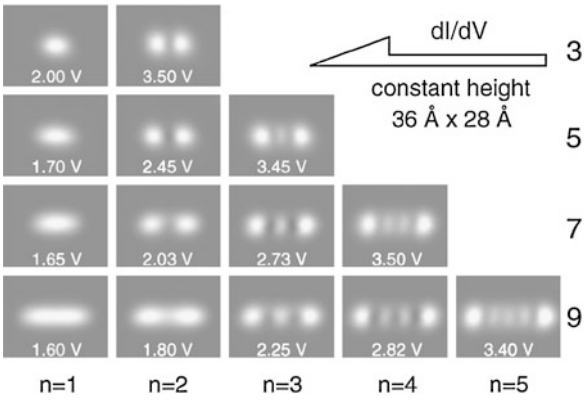

Fig. 19.10 CITS images obtained at constant distance and open feedback on copper chains on a Cu(111) surface. The images resemble the probability densities corresponding to the wave functions of electrons confined in a 1D potential well. Each *row* shows images of a Cu chain with given number of atoms indicated on the right. Each *column* refers to eigenstates with a fixed order n, specified at the *bottom of the column*. Adapted from [35]

all the $I(V)$ spectra, the corresponding tip-sample distances might be different because of topographical or electronic variations within the investigated sample area. Therefore, in some cases it might not be straightforward to relate CITS images measured in this way with 2D maps of the sample LDOS. The best method is to work with a fully disabled feedback, that is, at a true constant separation s. This type of measurements can however only be done if the surface topography is flat enough to avoid tip crashes and requires an extremely stable system and the absence of any drift. Figure 19.10 shows an example of CITS measurements done with this latter method on small chains of Cu atoms on a Cu(111) surface.

19.5.4 $s(V)$ Spectroscopy

In a $s(V)$ curve the tunnel current I is kept constant by using the feedback and the dependence of the tip-sample separation on the bias voltage is measured. As already explained in Sect. 19.5.2, this method allows a large dynamic range in V although spectral regions characterized by a low tunnel current are forbidden. In particular, $s(V)$ spectra are used to measure image-potential states whose energies lie above the vacuum barrier of the system and are therefore unaccessible to constant s spectroscopies. These bound states derive from the attractive potential existing between an electron approaching a metal surface and its positive image charge inside the metal. If their energies fall into a bulk band gap, the electrons cannot decay into bulk levels and are therefore trapped in these states. In presence of a STM tip, their position is Stark-shifted toward higher values due to the electric field between tip and sample. Image potential states can be detected as steps in a $s(V)$ curve [27, 36].

In fact, in order to keep a constant current, the tip retracts at voltages corresponding to successive image states, as the number of total states available to tunneling electrons increases.

19.5.5 $I(s)$ Spectroscopy

In a $I(s)$ curve the bias voltage V is kept constant and the tunneling current is measured as a function of the tip-sample distance. This type of spectroscopy is used to determine the height of the tunneling barrier and thus, through (19.9), the local work function of the surface. In fact, according to (19.14), the current depends on s only through the exponential factor e^{-2ks}. Thus, for small values of the bias voltage,

$$\left.\frac{dI}{ds}\right|_V \approx -2kI \tag{19.23}$$

or, using (19.11),

$$\frac{d\ln(I)}{ds} = \frac{1}{I}\frac{dI(s)}{ds} = -2k = -2\frac{\sqrt{2m\phi_A}}{\hbar}, \tag{19.24}$$

where ϕ_A is the apparent local barrier height, i.e. the barrier that the electron has to overcome during the tunneling. For distances $s > 5$ Å, ϕ_A is equal to the average work function $\overline{\phi} = (\phi_S + \phi_T)/2$ which, by inverting (19.24), can be expressed as

$$\overline{\phi} \approx 0.95\left(\frac{d\ln(I)}{ds}\right)^2, \tag{19.25}$$

where $\overline{\phi}$ is expressed in eV and s in Å. On the other hand, for distances $s < 5$ Å the attractive image potential (see Sect. 19.5.4) can no longer be neglected [37] and produces a decrease in the apparent local barrier height ϕ_A which is dependent on s. As a consequence, in this case the barrier ϕ_A measured with the $I(s)$ spectroscopy cannot be directly linked to the average work function $\overline{\phi}$ [37]. Moreover, for larger values of the bias voltage, band structure effects can further complicate the interpretation of the apparent local barrier height ϕ_A [38].

In analogy to what is done for $I(V)$ spectroscopy, also $I(s)$ spectra can be measured as a function of the lateral tip position. In this case, by assuming a constant tip work function, the resulting 2D maps can be interpreted as spatial variations of the sample work function [37, 39]. Similarly to what described in Sect. 19.5.3, dI/ds can be directly measured during constant current scanning, by modulating s with a small sinusoidal signal (typical values are a few tenths of an Å) at a frequency higher than the cut-off frequency of the feedback loop and by recording the output of the lock-in amplifier tuned on the first harmonic. The local sample work function can then be obtained from (19.25). Alternatively, in analogy to CITS measurements performed on a grid (Sect. 19.5.3), a full $I(s)$ spectrum at constant V can be recorded on a grid of points defined on a reference STM image. At each point of the grid, the feedback is switched off to perform the $I(s)$ measurement and then reactivated to continue recording the topographic image. An example of this type of measurement is shown in Fig. 19.11(b) for a PVBA molecule adsorbed on Cu(111).

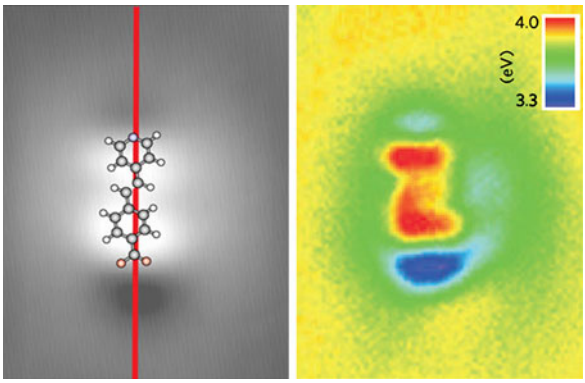

Fig. 19.11 (**a**) Constant-current STM image of a PVBA molecule adsorbed on Cu(111). (**b**) 2D map of the local potential barrier. Figures adapted by permission from Macmillan Publishers Ltd: Nature Materials [39], copyright 2010

19.5.6 Orbital Mediated Tunneling Spectroscopy

In 1989 Hipps [40] observed for the first time peaks in dI/dV spectra of molecules adsorbed on a metal surface. These peaks are due to a resonant tunneling mechanism via unoccupied or occupied molecular orbitals [41] and the spectroscopy that measures these transitions is called orbital mediated tunneling spectroscopy (OMTS). The mechanism of OMTS can be understood by considering the energy landscape experienced by a tunneling electron when there is a molecule between tip and sample. For a positive sample bias (Fig. 19.12(a)), the resonance conditions are met when the Fermi level of the tip matches the energy of an empty molecular orbital. At this voltage the tunneling current increases because a new pathway becomes available for the tunneling electrons (typical changes are around 10–30 %). In fact, besides the direct tip-sample tunneling process, also a tip-molecule-sample channel opens (Fig. 19.12(a)), therefore increasing the overall tunneling probability. At voltages above the resonance, this extra path is still available although, due to the conservation of energy, it can be used only by electrons whose energy is lower than E_F^T. These must overcome a higher tunneling barrier (see (19.10) and the discussion on the asymmetry of $I(V)$ spectra in Sect. 19.5.1) implying that the contribution of the empty molecular level to the overall conductivity becomes less effective. Essentially, the contribution is maximized at the resonance itself, thus producing a peak in the dI/dV characteristics. When the molecules are decoupled from the substrate (either by other molecules in multilayers [42] or by a thin insulating film [34]) the width of the molecular resonances narrows and the contribution from the direct tunneling into substrate states gets negligible. Under these conditions, the mechanism of resonant tunneling becomes the only viable conduction path for tip electrons and not only dI/dV but also I drops at voltages above the resonance. This produces the phenomenon of negative differential resistance (NDR) which is a proof of an effective molecular decoupling (see for example Fig. 19.13(a) for a bias of about 2 V).

For negative sample biases a similar tunneling mechanism is observed although the extra channels open when occupied molecular orbitals are moved into resonance

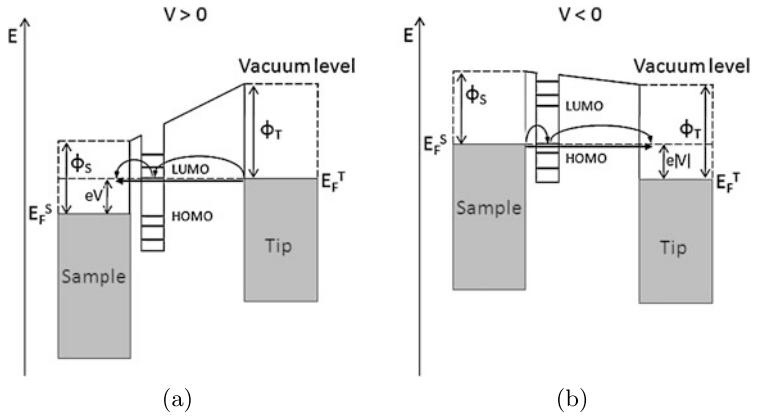

Fig. 19.12 Electron energy potential perpendicular to the surface when a molecule is located in the tip-sample gap. Resonant tunneling through unoccupied (**a**) and occupied (**b**) orbitals of an adsorbed molecule at positive and negative voltages, respectively

with the Fermi level of the tip (Fig. 19.12(b)). Finally, it should be noted that, by using a bias of a few Volts, it is possible to probe the occupied and unoccupied states of a large number of different types of molecules. However, for molecules with large energy gaps, the high voltage necessary for tunneling into the molecular states can significantly perturb the system or even break chemical bonds.

Peaks in OMTS spectra occur at voltages corresponding to resonance conditions and are due to the transition of electrons or holes through adsorbed molecules. The precise mechanism by which this happens depends on the details of the molecular electronic structure and of its coupling with both the sample and the tip. Two main scenarios can however be identified, depending on the residence time of the charge carrier onto the molecule [43]:

- Oxidation or reduction of the molecule followed by thermally induced return to the original charge state (electron hopping) [43, 44]. For a positive sample bias, an electron tunneling from the tip into an empty molecular state generates an anion which quickly relaxes into its new vibrational ground state. Successively, the extra electron tunnels from the molecule into the sample, thereby completing its conduction path. The molecule, reverted to the neutral state, relaxes back to its original ground state before a new electron restarts the cycle. Under these conditions, the rate of the reduction and oxidation processes is small enough that both the ion and the neutral molecule have time to completely relax their structure through the emission of photons or the coupling with the substrate phonons.
- Redox process occurring too rapidly for thermal relaxation to occur, such as in UPS or IPS [43]. In this case the electron residence time (10^{-15} s) is not long enough to allow the vibrational relaxation of the ion (10^{-13} s) which is thus formed in an excited state. This is similar to what happens in optical spectroscopy for a vertical transition in the Franck-Condon sense [43].

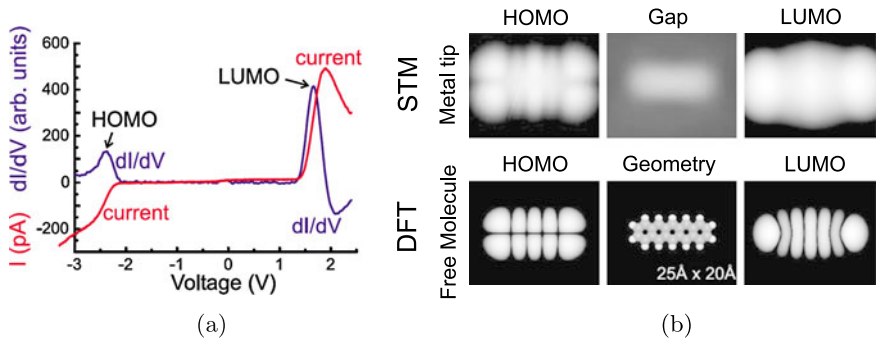

Fig. 19.13 (**a**) $I(V)$ and dI/dV spectra of a pentacene molecule adsorbed onto two layers on NaCl on Cu(111). Reprinted figure with permission from [34]. Copyright 2005 by the American Physical Society. (**b**) STM molecular orbital imaging. For a bias voltage corresponding to the HOMO and LUMO peaks in the dI/dV curve, the STM images resemble the spatial distribution of the HOMO and LUMO of the free molecule as calculated with DFT (*second row* in (**b**)). Figure adapted from [34]

The two different mechanisms lead to different positions of the observed peaks in the OMTS spectra. In fact, in the first case the measured energy corresponds to the difference between the bottoms of the potential energy surfaces of the ion and of the neutral molecule while, for a vertical transition, the difference is between an ionic excited level and the ground state of the neutral molecule.

OMTS spectroscopy of molecules that are effectively decoupled from the substrate can also be used to perform STM orbital imaging [34, 45]. As discussed above, in these conditions the tunneling current is mainly due to the molecular resonances which are energetically narrow and spatially localized. As a consequence, after the spectral position of a resonance has been identified in a dI/dV curve, a topographic image can be recorded at the corresponding bias voltage, thereby probing the spatial extension and shape of the associated molecular orbital. Due to the ultimate lateral resolution of STM, this can lead to intramolecular resolution of the orbital imaging. An example of this type of experiment is reported in Fig. 19.13 for the case of pentacene molecules adsorbed onto two layers of NaCl on Cu(111).

19.5.7 Inelastic Electron Tunneling Spectroscopy

So far we have assumed that electrons conserve their energy during the tunneling process, see (19.3). However, electrons can also tunnel inelastically between the tip and the sample exchanging energy and inducing the excitation of vibrational modes, spin-flips, magnons, plasmons, excitons, etc. either within the tunneling barrier (e.g. if there is a molecule between tip and sample) or in the electrodes themselves. These extra tunneling channels become available only above specific voltage thresholds $V^* = \hbar\omega/e$, where $\hbar\omega$ is the energy of the corresponding excitation. In fact, only

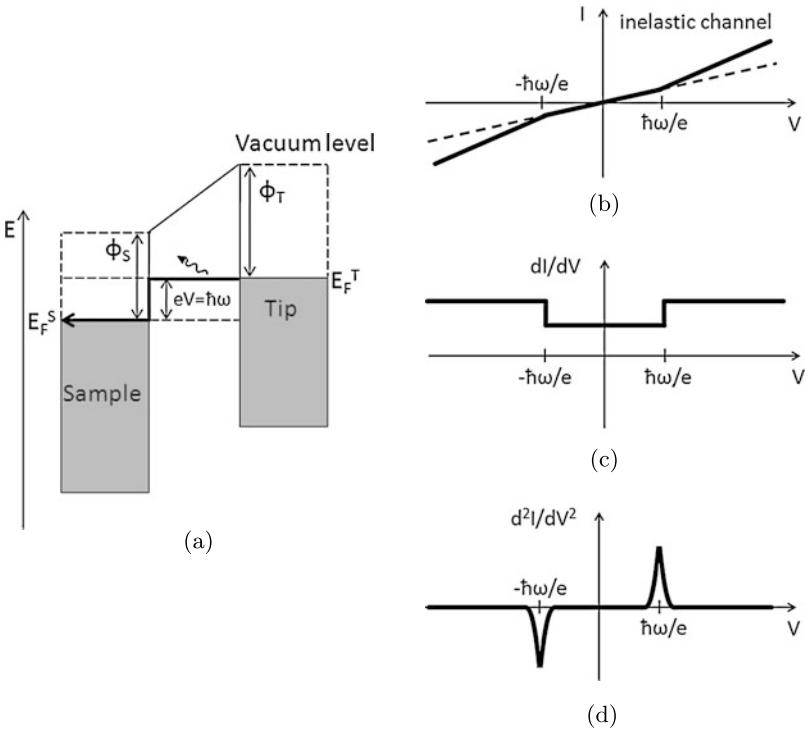

Fig. 19.14 Inelastic tunneling spectroscopy. (**a**) Schematic representation of the inelastic tunneling of electrons in a positively biased tip-vacuum-sample junction. (**b**)–(**d**) Corresponding effect on $I(V)$, dI/dV and d^2I/dV^2 spectra

beyond these values a part of the electron energy can be converted into the excitation.

The additional inelastic pathways increase the overall tunneling probability and therefore show up as discrete step-like features in the tunneling conductivity or as slope changes in $I(V)$ curves (Fig. 19.14(c) and (b), respectively). Note that this is different from the elastic tunneling case discussed in Sect. 19.5.6 since here the additional channel is available to any tunneling electron, provided its energy is larger than eV^*. However, normally, only 0.1 % of the electrons uses a vibrational inelastic channel and 5 % an electronic inelastic channel [43]. Due to this extremely low signal-to-background ratio, a lock-in technique becomes mandatory. In particular, the second harmonic component d^2I/dV^2 is measured as described in Sect. 19.3.2 since its plot versus V displays onsets of inelastic channels as peaks (Fig. 19.14(d)). This technique is called inelastic tunneling spectroscopy (IETS).

The extra inelastic channels are accessible both to electrons tunneling from the tip to the sample and to electrons following the reverse path. As a consequence, the corresponding peaks in the d^2I/dV^2 spectrum appear at the same voltage independent of sign, even if the intensities can be different due to the different density

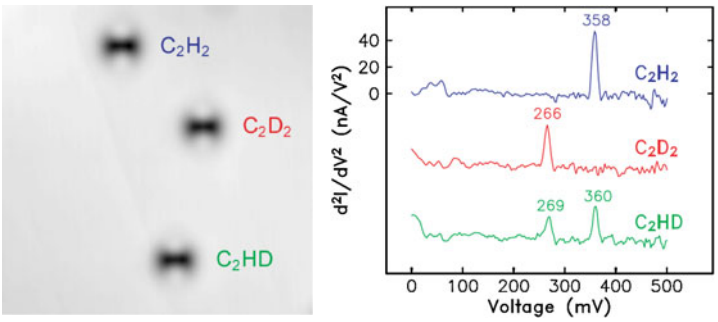

Fig. 19.15 (**a**) STM images and (**b**) STM-IETS spectra of three isotopes of acetylene on Cu(001) at 8 K. Reprinted with permission from [50]. Copyright 2002, American Institute of Physics

of states of the two electrodes. The exhibition of this symmetry is considered as the necessary fingerprint to assign specific spectral features to inelastic processes. A high spectral resolution is particularly important in IETS since the energetic separation of several inelastic processes is very small (e.g. less than 1 meV for spin flips [46], a few tenths of a meV for vibrational modes [47, 48]). As a consequence, apart from minimizing any type of instrumental broadening, IETS measurements have to be performed at cryogenic temperatures since the intrinsic line width is at least 5.4 kT due to the thermal broadening of the Fermi-Dirac distributions [8] (as a reference, 5.4 kT is equal to 0.3 meV at $T = 0.6$ K and to 140 meV at $T = 300$ K).

IETS benefits from the same spatial resolution as STM and STS and has therefore been used to measure vibrational modes of individual molecules, spin excitations of single magnetic atoms, collective plasmon excitations in 2D materials and magnons in ferromagnets on the sub-nm scale. An example of the possibilities of IETS is demonstrated in Fig. 19.15 for the vibrational excitations of single molecules. The STM image in Fig. 19.15(a) displays three apparently identical acetylene molecules. However, upon analysis of the corresponding IETS spectra (Fig. 19.15(b)), these are revealed as three differently deuterated isotopes, C_2H_2, C_2D_2 and C_2HD [49]. Similarly to other vibrational spectroscopy techniques such as infrared or Raman, IETS spectra show the isotope shifts in the C–H or C–D stretches. The essential difference of this type of measurements is the ability of doing so on individual molecules.

A different way of detecting tunneling-induced molecular vibrations by means of STM is to rely on their coupling with dynamical processes such as molecular motions. In particular, by placing the STM tip over a target molecule, a vibrational mode and an associate molecular motion can be excited by inelastically tunneling electrons if the bias voltage is increased above the corresponding threshold. By measuring the frequency of molecular diffusion events as a function of the time, the applied bias voltage and the tunneling current, it is possible to create so-called *action spectra* which reflect the vibrational spectrum of an individual molecule in a quantitative manner [51].

Optical excitations can also be revealed in an alternative way by coupling the STM with a photon detection system able to collect and analyze the luminescence stimulated by inelastic electrons [52, 53]. Such a setup has been used to characterize plasmon emission from metallic surfaces and luminescence from semiconductor quantum structures and adsorbed molecules [54, 55].

19.6 Tip-Induced Modification

Besides being an extraordinary instrument for the characterization of structural, electronic, vibrational, optical and magnetic properties of surfaces with subnanometer resolution, STM has also developed as a tool to modify and nano-engineer matter at the single molecule and atom scale.

By decreasing the distance between the tip and the sample in a controlled way, indentations can be produced in the substrate with lateral sizes down to a few nm. Nanolithography can also be performed by tunneling electrons into a layer of e-beam photoresist, thereby reaching a better resolution compared to standard electron beam lithography [56]. Many other STM-based nanopatterning and nanofabrication techniques have been developed based on a number of physical and chemical principles [57–60] including anodic oxidation, field evaporation, selective chemical vapor deposition, selective molecular desorption, electron-beam induced effects and mechanical contact. All these methods exploit the extreme lateral localization of the tunneling current and can be applied in air, liquids and vacuum.

However, the nanotechnological application that gained most attention is the ability to manipulate individual atoms and molecules on a substrate. This is possible due to a controlled use of tip-particle forces and is typically done in UHV and at low temperatures. The first atomic manipulation experiment was performed by Eigler and Schweizer in 1989 [2]. This phenomenal result fulfilled Richard Feynman's prophecy that "ultimately-in the great future-we can arrange the atoms the way we want; the very atoms, all the way down!" [3].

During a lateral manipulation experiment the tip is first placed above the particle to be moved (for example an atom) and the tunneling current is increased while keeping a constant voltage. This results in a movement of the tip toward the atom, see (19.14). If their separation is sufficiently reduced, Van der Waals forces start to come into play together with attractive and repulsive chemical interactions. When these forces equal the diffusion energy barrier, a lateral displacement of the tip can induce a movement of the atom parallel to the surface. Upon reaching the desired final position, the tip is retracted by reducing the tunneling current to the initial value, leaving the atom in the selected place. Depending on the tip-particle distance and therefore on the strength and nature of the interaction, different manipulation modes including pulling, pushing and sliding [61] were identified and used to move different types of atoms and molecules. It is worth to notice that this type of manipulation is not influenced by the value of the voltage bias.

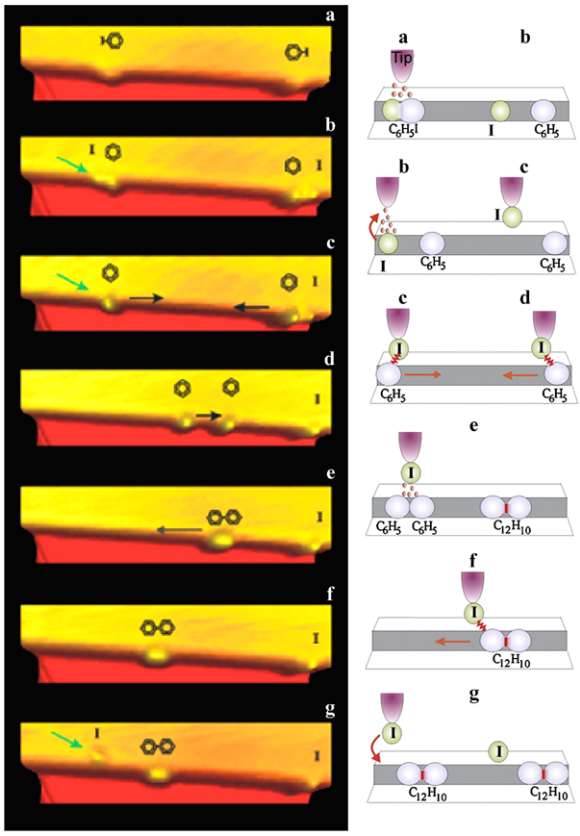

Fig. 19.16 STM images and schematics of the steps of the STM-tip induced Ullmann reaction on Cu(111). Adapted from [70]

Thanks to this technique, it was possible to fabricate artificial nanostructures such as the *quantum corral* [62] and to probe quantum mechanical effects like the quantum confinement of surface state electrons or the *quantum mirage* [63]. Lateral STM manipulation has also been used to switch between different adsorption configurations and conformations of molecules on surfaces and to modify their electronic properties in a controlled way [64].

A further application of STM manipulation is the synthesis of new molecular species based on the ability of STM to form and break chemical bonds with atomic precision. Reactants are brought close together on the surface and the actual reaction is realized by applying a voltage pulse or by exciting vibrational modes through inelastically tunneling electrons. Examples of this technique include the dissociation of diatomic molecules [65], the Ullmann reaction (Fig. 19.16) [66], the isomerization of dichlorobenzene [67] and the creation of metal-ligand complexes [68, 69].

The STM tip has also been used to perform vertical manipulations of nanoparticles where an atom (or molecule) is deliberately transfered from the surface to the tip and vice versa by using the electric field generated by the bias voltage. In contrast to the lateral manipulation, here the bonds between the surface and the atom are

Fig. 19.17 (**a**) Chemical structure of PTCDA. (**b**) STM and (**c**) STHM image of a PTCDA molecule adsorbed on Au(111). Adapted from [73]

broken and re-created [71]. By approaching the tip at distances of a few Å from the chosen particle, new interactions are established that reduce the atom-surface binding energy. If a voltage pulse is applied under these conditions, the resulting electric field (of the order of 10^8 V/cm) can be enough to induce the particle desorption. The vertical manipulation technique has also been used as a means to increase the lateral resolution of STM. In fact, the controlled adsorption of a specific molecule onto the tip often makes it "sharper" and can add a chemical resolution capability if the DOS of the extra molecule acts as an "energy filter" [34].

A related effect is exploited in the recently proposed scanning tunneling hydrogen microscopy (STHM) technique [73]. In STHM the experimental chamber is flooded with molecular hydrogen while the tip is scanned in constant height mode at a very close distance over the surface. H_2 can get trapped in the tip-sample junction and its rearrangement during scanning of the surface generates a new contrast mechanism based on the short-range Pauli repulsion. This is extremely sensitive to the total electron density, thereby endowing the STM with similar imaging capabilities to non-contact AFM [72] and making it able to resolve the inner structure of complex organic molecules [73] (Fig. 19.17(c)). This is not the case for standard STM which, being mainly influenced by the frontier molecular orbitals, reproduces their spatial distribution. In particular, if the molecule is adsorbed on a metallic substrate, the metal-organic interaction can lead to a substantial broadening and restructuring of the molecular orbitals which become spatially delocalized (Fig. 19.17(b)).

Acknowledgements This work was supported by EPSRC (EP/D000165/1); A. Della Pia was funded through a WPRS scholarship of the University of Warwick.

References

1. G. Binnig, H. Rohrer, C. Gerber, E. Weibel, Phys. Rev. Lett. **49**(1), 57 (1982)
2. D.M. Eigler, E.K. Schweizer, Nature **344**(6266), 524 (1990)
3. R.P. Feynman, J. Microelectromech. **1**(1), 60 (1992)
4. J. Bardeen, Phys. Rev. Lett. **6**(2), 57 (1961)
5. A.D. Gottlieb, L. Wesoloski, Nanotechnology **17**(8), R57 (2006)
6. N.D. Lang, Phys. Rev. B **34**(8), 5947 (1986)
7. L.D. Landau, E.M. Lifshitz, *Quantum Mechanics. Non-relativistic Theory* (Pergamon Press, Oxford, 1977)

8. C.J. Chen, *Introduction to Scanning Tunneling Microscopy* (Oxford University Press, New York, 2008)
9. G. Binnig, H. Rohrer, Helv. Phys. Acta **55**(6), 726 (1982)
10. A. Okumura, K. Miyamura, Y. Gohshi, J. Microsc. **152**(3), 631 (1988)
11. K. Besocke, Surf. Sci. **181**(1–2), 145 (1987)
12. S.H. Pan, E.W. Hudson, J.C. Davis, Rev. Sci. Instrum. **70**(2), 1459 (1999)
13. E. Meyer, H.J. Hug, R. Bennewitz, *Scanning Probe Microscopy: The Lab on a Tip* (Springer, Berlin, 2004)
14. I. Ekvall, E. Wahlstrom, D. Claesson, H. Olin, E. Olsson, Meas. Sci. Technol. **10**(1), 11 (1999)
15. J.P. Ibe, P.P. Bey, S.L. Brandow, R.A. Brizzolara, N.A. Burnham, D.P. Dilella, K.P. Lee, C.R.K. Marrian, R.J. Colton, J. Vac. Sci. Technol. A **8**(4), 3570 (1990)
16. L.A. Nagahara, T. Thundat, S.M. Lindsay, Rev. Sci. Instrum. **60**(10), 3128 (1989)
17. E. Laegsgaard, L. Osterlund, P. Thostrup, P.B. Rasmussen, I. Stensgaard, F. Besenbacher, Rev. Sci. Instrum. **72**(9), 3537 (2001)
18. M.J. Rost, L. Crama, P. Schakel, E. van Tol, G.B.E.M. van Velzen-Williams, C.F. Overgauw, H. ter Horst, H. Dekker, B. Okhuijsen, M. Seynen, A. Vijftigschild, P. Han, A.J. Katan, K. Schoots, R. Schumm, W. van Loo, T.H. Oosterkamp, J.W.M. Frenken, Rev. Sci. Instrum. **76**(5), 053710 (2005)
19. L. Petersen, M. Schunack, B. Schaefer, T.R. Linderoth, P.B. Rasmussen, P.T. Sprunger, E. Laegsgaard, I. Stensgaard, F. Besenbacher, Rev. Sci. Instrum. **72**(2), 1438 (2001)
20. T. Zambelli, J.V. Barth, J. Wintterlin, G. Ertl, Nature **390**(6659), 495 (1997)
21. C. Klink, L. Olesen, F. Besenbacher, I. Stensgaard, E. Laegsgaard, N.D. Lang, Phys. Rev. Lett. **71**(26), 4350 (1993)
22. F.E. Olsson, M. Persson, N. Lorente, L.J. Lauhon, W. Ho, J. Phys. Chem. B **106**(33), 8161 (2002)
23. J. Tersoff, D.R. Hamann, Phys. Rev. Lett. **50**(25), 1998 (1983)
24. P. Sautet, J. Dunphy, D.F. Ogletree, M. Salmeron, Surf. Sci. **295**(3), 347 (1993)
25. J.A. Stroscio, R.M. Feenstra, A.P. Fein, Phys. Rev. Lett. **57**(20), 2579 (1986)
26. M. Passoni, F. Donati, A.L. Bassi, C.S. Casari, C.E. Bottani, Phys. Rev. B **79**(4), 045404 (2009)
27. J.A. Stroscio, W.J. Kaiser, *Scanning Tunneling Microscopy* (Academic Press, London, 1993)
28. P. Wahl, L. Diekhoner, M.A. Schneider, K. Kern, Rev. Sci. Instrum. **79**(4), 043104 (2008)
29. B. Koslowski, C. Dietrich, A. Tschetschetkin, P. Ziemann, Phys. Rev. B **75**(3), 035421 (2007)
30. M. Ziegler, N. Neel, A. Sperl, J. Kroger, R. Berndt, Phys. Rev. B **80**(12), 125402 (2009)
31. B. Koslowski, H. Pfeifer, P. Ziemann, Phys. Rev. B **80**(16), 165419 (2009)
32. B. Naydenov, J.J. Boland, Phys. Rev. B **82**(24), 245411 (2010)
33. C. Wagner, R. Franke, T. Fritz, Phys. Rev. B **75**(23), 235432 (2007)
34. J. Repp, G. Meyer, S.M. Stojkovic, A. Gourdon, C. Joachim, Phys. Rev. Lett. **94**(2), 026803 (2005)
35. S. Folsch, P. Hyldgaard, R. Koch, K.H. Ploog, Phys. Rev. Lett. **92**(5), 056803 (2004)
36. G. Binnig, K.H. Frank, H. Fuchs, N. Garcia, B. Reihl, H. Rohrer, F. Salvan, A.R. Williams, Phys. Rev. Lett. **55**(9), 991 (1985)
37. R. Wiesendanger, *Scanning Probe Microscopy and Spectroscopy: Methods and Applications* (Cambridge University Press, Cambridge, 1994)
38. M. Becker, R. Berndt, Phys. Rev. B **81**(3), 035426 (2010)
39. L. Vitali, G. Levita, R. Ohmann, A. Comisso, A. De Vita, K. Kern, Nat. Mater. **9**(4), 320 (2010)
40. K.W. Hipps, J. Phys. Chem. **93**(16), 5958 (1989)
41. W. Mizutani, M. Shigeno, K. Kajimura, M. Ono, Ultramicroscopy **42**(a), 236 (1992)
42. M. Grobis, A. Wachowiak, R. Yamachika, M.F. Crommie, Appl. Phys. Lett. **86**(20), 204102 (2005)
43. K.W. Hipps, Scanning tunneling spectroscopy (STS), in *Handbook of Applied Solid State Spectroscopy*, ed. by D.R. Vij (Springer, New York, 2006)
44. U. Mazur, K.W. Hipps, J. Phys. Chem. B **103**(44), 9721 (1999)

45. J. Repp, G. Meyer, S. Paavilainen, F.E. Olsson, M. Persson, Science **312**(5777), 1196 (2006)
46. A.J. Heinrich, J.A. Gupta, C.P. Lutz, D.M. Eigler, Science **306**(5695), 466 (2004)
47. N. Lorente, M. Persson, Phys. Rev. Lett. **85**(14), 2997 (2000)
48. L. Vitali, M.A. Schneider, K. Kern, L. Wirtz, A. Rubio, Phys. Rev. B **69**(12), 121414 (2004)
49. B.C. Stipe, M.A. Rezaei, W. Ho, Science **280**(5370), 1732 (1998)
50. W. Ho, J. Chem. Phys. **117**(24), 11033 (2002)
51. Y. Sainoo, Y. Kim, T. Okawa, T. Komeda, H. Shigekawa, M. Kawai, Phys. Rev. Lett. **95**(24), 246102 (2005)
52. J.K. Gimzewski, B. Reihl, J.H. Coombs, R.R. Schlittler, Z. Phys. B, Condens. Matter **72**(4), 497 (1988)
53. J.G. Keizer, J.K. Garleff, P.M. Koenraad, Rev. Sci. Instrum. **80**(12), 123704 (2009)
54. F. Rossel, M. Pivetta, W.D. Schneider, Surf. Sci. Rep. **65**(5), 129 (2010)
55. P. Bharadwaj, A. Bouhelier, L. Novotny, Phys. Rev. Lett. **106**(22), 226802 (2011)
56. R.F.W. Pease, J. Vac. Sci. Technol. B **10**(1), 278 (1992)
57. H. Iwasaki, T. Yoshinobu, K. Sudoh, Nanotechnology **14**(11), R55 (2003)
58. H.J. Mamin, P.H. Guethner, D. Rugar, Phys. Rev. Lett. **65**(19), 2418 (1990)
59. C.F. Quate, Surf. Sci. **386**(1–3), 259 (1997)
60. C. Shen, M. Buck, Nanotechnology **20**(24), 245306 (2009)
61. L. Bartels, G. Meyer, K.H. Rieder, D. Velic, E. Knoesel, A. Hotzel, M. Wolf, G. Ertl, Phys. Rev. Lett. **80**(9), 2004 (1998)
62. M.F. Crommie, C.P. Lutz, D.M. Eigler, Science **262**(5131), 218 (1993)
63. H.C. Manoharan, C.P. Lutz, D.M. Eigler, Nature **403**(6769), 512 (2000)
64. F. Moresco, G. Meyer, K.H. Rieder, H. Tang, A. Gourdon, C. Joachim, Phys. Rev. Lett. **86**(4), 672 (2001)
65. B.C. Stipe, M.A. Rezaei, W. Ho, S. Gao, M. Persson, B.I. Lundqvist, Phys. Rev. Lett. **78**(23), 4410 (1997)
66. S.W. Hla, L. Bartels, G. Meyer, K.H. Rieder, Phys. Rev. Lett. **85**(13), 2777 (2000)
67. K. Morgenstern, Acc. Chem. Res. **42**(2), 213 (2009)
68. P. Liljeroth, I. Swart, S. Paavilainen, J. Repp, G. Meyer, Nano Lett. **10**(7), 2475 (2010)
69. N. Katsonis, J. Vicario, T. Kudernac, J. Visser, M.M. Pollard, B.L. Feringa, J. Am. Chem. Soc. **128**(48), 15537 (2006)
70. K.H. Rieder, G. Meyer, F. Moresco, K. Morgenstern, S.W. Hla, J. Repp, M. Alemani, L. Grill, L. Gross, M. Mehlhorn, H. Gawronski, V. Simic-Milosevich, J. Henzl, K.F. Braun, S. Foelsch, L. Bartels, in *Conference on Atoms and Molecules Near Surfaces*, ed. by L.F.J. Weiner, J. Schmiedmayer. Journal of Physics Conference Series, vol. 19 (IOP Publishing, Bristol, 2005), p. 175
71. P. Avouris, Acc. Chem. Res. **28**(3), 95 (1995)
72. L. Gross, F. Mohn, N. Moll, P. Liljeroth, G. Meyer, Science **325**(5944), 1110 (2009)
73. C. Weiss, C. Wagner, C. Kleimann, M. Rohlfing, F.S. Tautz, R. Temirov, Phys. Rev. Lett. **105**(8), 086103 (2010)